OXFORD

Cerebral Cortex, 2024, **34**, 1–13
https://doi.org/10.1093/cercor/bhad499
Advance access publication date 6 January 2024
Original Article

Cortical atrophy in early-stage patients with anti-NMDA receptor encephalitis: a machine-learning MRI study with various feature extraction

Sisi Shen[1,†], Ran Wei[2], Yu Gao[2], Xinyuan Yang[2], Guoning Zhang[2], Bo Yan[2], Zhuoling Xiao[2,*,†], Jinmei Li[1,*]

[1]Department of Neurology, West China Hospital of Sichuan University, 37 GuoXue Alley, Chengdu 610041, China,
[2]School of Information and Communication Engineering, University of Electronic Science and Technology of China No.2006, Xiyuan Ave, West Hi-Tech Zone, 611731| Chengdu, Sichuan, P.R. China

*Corresponding authors: Jinmei Li, Department of Neurology, West China Hospital of Sichuan University, Chengdu, 610041, China. Email: lijinmei@wchscu.cn; Zhuoling Xiao, School of Information and Communication Engineering, University of Electronic Science and Technology of China No.2006, Xiyuan Ave, West Hi-Tech Zone, 611731 | Chengdu, Sichuan, P.R. China. Email: zhuolingxiao@uestc.edu.cn

†Sisi Shen and Zhuoling Xiao contributed equally to this work and should be considered as co-first author.

Conventional brain magnetic resonance imaging (MRI) of anti-N-methyl-D-aspartate-receptor encephalitis (NMDARE) is non-specific, thus showing little differential diagnostic value, especially for MRI-negative patients. To characterize patterns of structural alterations and facilitate the diagnosis of MRI-negative NMDARE patients, we build two support vector machine models (NMDARE versus healthy controls [HC] model and NMDARE versus viral encephalitis [VE] model) based on radiomics features extracted from brain MRI. A total of 109 MRI-negative NMDARE patients in the acute phase, 108 HCs and 84 acute MRI-negative VE cases were included for training. Another 29 NMDARE patients, 28 HCs and 26 VE cases were included for validation. Eighty features discriminated NMDARE patients from HCs, with area under the receiver operating characteristic curve (AUC) of 0.963 in validation set. NMDARE patients presented with significantly lower thickness, area, and volume and higher mean curvature than HCs. Potential atrophy predominately presented in the frontal lobe (cumulative weight = 4.3725, contribution rate of 29.86%), and temporal lobe (cumulative weight = 2.573, contribution rate of 17.57%). The NMDARE versus VE model achieved certain diagnostic power, with AUC of 0.879 in validation set. Our research shows potential atrophy across the entire cerebral cortex in acute NMDARE patients, and MRI machine learning model has a potential to facilitate the diagnosis MRI-negative NMDARE.

Key words: machine learning; SVM; patterns of structural alterations; anti-NMDA receptor encephalitis.

Introduction

Anti-NMDA receptor (N-methyl-D-aspartate-receptor, NMDAR) encephalitis (NMDARE) is the most common autoimmune encephalitis characterized by rapidly deteriorating psychiatric symptoms, seizures, amnesia, dyskinesia, autonomic instability, catatonia, mutism, and a decreased level of consciousness (Venkatesan and Adatia 2017; Baumgartner et al. 2019; Dalmau et al. 2019). Initial clinical manifestations of NMDARE are very similar with viral encephalitis (VE), an acute infectious disease of the central nervous system caused by virus infection, making it difficult to distinguish them in the early stage clinically. A total of 70% of NMDARE patients are admitted to intensive care units (ICU) for airway protection, coma, refractory status epilepticus or breathing dysfunction (Titulaer et al. 2013; de Montmollin et al. 2017), while the rate of ICU admission among VE patients is about 25% (Thakur et al. 2013; Sonneville et al. 2015). Although the condition of NMDARE is severe, less than 50% patients show abnormal magnetic resonance imaging (MRI) images (Dalmau et al. 2011; Titulaer et al. 2013; Barry et al. 2015; Bacchi et al. 2018), while MRI abnormalities were more frequent in VE (Bani-Sadr et al. 2023; Tan et al. 2023). This may be associated with the mechanisms of these two encephalitis. Previous pathogenesis studies of NMDARE have shown that the GluN1 antibody crosses the impaired blood brain barrier and is directly pathogenic by downregulating neuronal NMDARs and disrupting synaptic NMDAR currents, which leads to the change of neuron membrane receptor, synaptic protein function, but less neuron necrosis and microbleeds (Dalmau et al. 2007; Kreye et al. 2016; Malviya et al. 2017). VE is caused by virus invasion into brain parenchyma, which leads to the direct destruction of tissues and a large number of neuron necrosis and hemorrhage (Shives et al. 2017). Regarding immune therapy, including corticosteroids, intravenous immunoglobulins or plasma exchange, 75% of NMDARE patients experienced complete or near-complete recovery (Dalmau et al. 2008; Gable et al. 2009; Dalmau et al. 2011; Finke et al. 2012). The prognosis of patients depends on early diagnosis and the implementation of appropriate immunomodulatory therapy (Finke et al. 2012; Titulaer et al. 2013). In cases where treatment is delayed or ineffective, the mortality rate of NMDARE may be very high (12% to 100%) (Day et al. 2011; Singh et al. 2015). These observations stress the importance of early diagnosis of NMDARE. But antibody tests are not readily available everywhere and results can take several weeks (Graus et al. 2016).

MRI is widely used as a component of the workup for the diagnosis of encephalopathy in primary centers. However, visual inspection of MRI demonstrated that 50% to 70% of NMDARE patients showed MRI-negative images (no lesions in conventional magnetic resonance sequences, such as T1-weighted (T1WI), T2-weighted (T2WI) and fluid-attenuated inversion recovery (FLAIR) sequences), thus showing little usefulness as biomarkers for the

Received: August 10, 2023. **Revised:** November 29, 2023. **Accepted:** November 30, 2023

diagnosis of NMDARE (Barry et al. 2015). The conversion of MR images into high-dimensional, minable, and quantitative imaging features via high-throughput extraction of data-characterization algorithms, machine learning of MRI data can supply large amounts of information that are invisible to the human eye. Using machine-learning analysis of MRI data, researchers can identify significant structural and functional differences between healthy and diseased individuals or between diseased individuals. These differences are considered to be imaging biomarkers that contain discriminative information and have been successfully applied in the identification of many neuropsychiatric diseases. Jiajie Mo et al. employed support vector machine (SVM) model to detect hippocampal sclerosis (HS) and to explore the characteristics of structural alterations of HS from 79 radiomics features of hippocampus extracted from FreeSurfer software in 80 histologically proven HS patients and 80 healthy controls (HCs). The result showed that the SVM model was valuable in clinical practice for improving the detection rate of MRI-negative HS to 96% (Mo et al. 2019). de Pierrefeu et al. 2018 proposed SVM algorithm in 276 schizophrenia patients and 330 HCs to identify neuroanatomical signature of schizophrenia. They found machine learning classifiers yield significant inter-site prediction accuracies (72%) together with an excellent predictive signature stability. Machine-learning analysis of MRI data also has been applied in focal cortical dysplasia (Mo et al. 2018) and Alzheimer's disease (Acharya et al. 2019).

In 2022, Jinping Xu used general linear model and brain MRI data during the recovery period (mean time between first symptom and imaging is 15.16 months) to investigate structural morphology alterations in 24 NMDARE patients by comparing with 30 HCs, and found that patients showed significantly decreased cortical alterations mainly in language network and default mode network, as well as decreased gray matter volume in left cornu ammonis 1 body of hippocampus, which was associated with cognitive impairments resulted from long-term sequelae of the encephalitis and can be served as effective features to assess disease progression (Xu et al. 2022). To the best of our knowledge, no previous studies have specifically applied machine learning of MRI data in acute MRI-negative NMDARE patients. We hypothesize that machine learning of MRI data can facilitate the diagnosis of NMDARE presenting with negative brain MRI and produce imaging biomarkers for NMDARE. Therefore, we build machine learning models for (i) MRI- negative NMDARE patients versus HCs and (ii) MRI- negative NMDARE patients versus MRI- negative VE patients based on their brain MRI and extract MRI features that could discriminate MRI-negative NMDARE patients from HCs and MRI- negative VE patients.

Method

Participants

In training stage, two datasets were recruited. One was for MRI-negative NMDARE versus HCs model and one was for MRI-negative NMDARE versus MRI- negative VE model. Only MRI-negative patients with high-quality brain MRI images would be included in both datasets. This was evaluated by two experienced neurologists (both with 10 years of experience). Images with no motion artifacts, aliasing, or rippling related to eye movement and can be processed by FreeSurfer (structural MRI analysis software) were considered as high-quality. No lesions on T1WI, T2WI, and FLAIR sequence were considered MRI-negative. After image evaluating, all MRI-negative NMDARE patients referred to our department between 2010 January 1st and 2019 August 31st were included in both datasets as cases. Age- and sex-matched HCs retrospectively selected from our healthy volunteer database recruited from the general population, who have no history of any neurological or psychiatric disorders, head trauma or other major medical conditions, were included in MRI-negative NMDARE versus HCs datasets as controls. Age- and sex-matched MRI-negative acute VE patients referred to our department were included in MRI-negative NMDARE versus MRI-negative VE dataset as controls. The range used to match subjects for age was ±3 years. In testing stage, MRI-negative NMDARE attending between 2019 August 31st and 2020 August 31st and another MRI-negative acute VE patients and HCs were recruited for validation. The validation set patients were independent from the training set patients.

In this study, we included 109 MRI-negative NMDARE patients and 108 age- and sex-matched HCs in MRI-negative NMDARE versus HC training dataset. And in MRI-negative NMDARE versus MRI-negative VE training dataset, 109 MRI-negative NMDARE patients and 84 age- and sex-matched MRI-negative acute VE patients were included. For validation, 29 MRI-negative NMDARE patients and 28 HCs were included in NMDARE versus HC testing dataset. And 29 MRI-negative NMDARE patients and 26 MRI-negative acute VE patients were included in NMDARE versus VE testing dataset.

Diagnostic criteria

The diagnosis of NMDARE was based on the presence of one or more of the six major groups of symptoms (abnormal psychiatric behavior or cognitive dysfunction; speech dysfunction; seizures; movement disorder, dyskinesias, or rigidity/abnormal postures; decreased level of consciousness; autonomic dysfunction or central hypoventilation) together with the presence of IgG antibodies for NMDA receptors (Graus et al. 2016).

According to the International Encephalitis Consortium, VE is diagnostically defined as a persistent altered mental status (altered level of consciousness or personality change) lasting more than 24 h without encephalopathy from other causes with at least three of the following associated manifestations: fever within 72 h before and after the onset of symptoms (>38°C), generalized or partial seizures not fully attributable to a preexisting seizure disorder, new onset of focal neurological deficits, increased white blood cell count in the CSF ($\geq$5/mm^3), and imaging/EEG results consistent with changes associated with encephalitis (Venkatesan et al. 2013).

Inclusion/exclusion criteria

Inclusion criteria: (i) Patients' serum and cerebrospinal fluid (CSF) antibodies against the NMDA receptor were confirmed by a cell-based indirect immune-fluorescence test (IIFT) employing BIOCHIPs (EUROIMMUN AG, Luebeck, Germany) in either the laboratory of Peking Union Medical College Hospital or the EUROIMMUN Diagnostic Laboratory in China; (ii) NMDARE and VE according diagnostic criteria; (iii) MRI scan within 3 days after admission and 90 days from symptom onset; (iv) High-quality 3.0 T brain MRI imaging data (i.e. no motion artifacts, aliasing, or rippling related to eye movement and can be processed by image analysis software); and v) MRI-negative patients (no lesions on magnetic resonance conventional sequence, such as T1WI, T2WI, and FLAIR.

Exclusion Criteria: (i) Patients with other central nervous system diseases, such as metabolic encephalopathy, and neurodegenerative diseases and (ii) patients whose MRI scans with severe motion artifacts, aliasing, or rippling related to eye movement

Table 1. The number of included patients and HCs scanned in each scanner.

Scanner	Training cohorts			Testing cohorts		
	NMDARE	VE	HCs	NMDARE	VE	HCs
Trio	11	8	10	3	2	2
Skyra	98	76	98	26	24	27

NMDAR, N-methyl-D-aspartate receptor; VE, viral encephalitis; HCs, Health controls

or MRI scans are incomplete or can't be processed by imaging software.

The ethics committee of West China Hospital approved the study (Nos. 2020-1310).

Clinical data

Two experienced neurologists specializing in encephalitis collected information from medical records about demographics, symptom onset date, admission date, MRI scan date, imaging features, laboratory features and CSF and serum anti-NMDAR antibody. Ambiguous or unclear information was excluded from analysis.

MRI acquisition

All patients underwent a structural MRI (sMRI) in the acute phase (during hospitalization). The sMRI images for all of the subjects were acquired using a Trio or Skyra 3.0 T scanner (Siemens, Erlangen, Germany). T1WI was collected using spin echo for good contrast between the gray and white matter and short scan time which is suitable for encephalitis patients in the acute phase, who are not tolerating long-time MRI scan. The following parameters were used: repetition time = 450 to 500 ms, echo time = 10 to 12 ms, slice thickness = 5.0 mm, matrix = 256 × 256, and number of axial slices = 20. Axial T2WI and FLAIR were also acquired in the clinical protocol. The number of included patients and HCs scanned in each scanner are shown in Table 1.

MRI data processing (feature extraction)

Before MRI data processing, two experienced neurologists (both with 10 years of experience) assessed the structural images quality visually. Only images with no motion artifacts, aliasing, or rippling related to eye movement and no lesions on T1WI, T2WI, and FLAIR sequence (MRI-negative) were included in this study.

T1WI images of included subjects were used for analysis. Segmentation of T1WI images was performed using FreeSurfer version 7.1.1 (http://surfer.nmr.mgh.harvard.edu/), which has been validated against histological measurements and demonstrates good test–retest reliability. The pipeline in FreeSurfer provided a full processing stream for structural images, including skull stripping, B1 bias field correction, and gray–white matter segmentation; reconstruction of cortical surface models (gray–white boundary surface and pial surface); labeling of regions on the cortical surface, as well as subcortical brain structures; nonlinear registration of the cortical surface of an individual with a stereotaxic atlas; reconstruction of the cerebral cortex and the establishment of a surface map to calculate the cortical characteristic parameters of each brain area. Subjects whose images can't be processed by FreeSurfer and whose reconstruction results were considered to be untrustworthy in visual inspection were discarded from the study.

By using FreeSurfer's automatic reconstruction procedure, the brain regions were segmented into 148 cortical regions (74 regions per hemisphere) and 50 subcortical regions of interest using the Destrieux 2009 Atlas and the Aseg-Subcortical Atlas (https://surfer.nmr.mgh.harvard.edu/fswiki/CorticalParcellation; https://surfer.nmr.mgh.harvard.edu/fswiki/SubcorticalSegmentation, details are shown in Supplementary Table 1). Four features (volume, thickness, surface area, and mean curvature) were extracted for each cortical region (592 cortical region features in total), and volume feature was extracted for each subcortical region (50 subcortical region features). Along with the estimated total intracranial volume, volume of all voxels without ventricles (BrainSegVolNotVent), bilateral white surface area, and bilateral mean thickness, 648 features were extracted from each individual's MRI imaging data.

Feature selection

Since selecting features for classification based on the results of group tests (mostly Student's t-test) that were conducted on the whole dataset is a form of double dipping and therefore leads to biased (inflated) results (Demirci et al. 2008) and the loss of valuable discriminatory information (Arbabshirani et al. 2017), support vector machine-recursive feature elimination (SVM-RFE) algorithm was adopted to select features. It is a popular wrapper method that can result in superior performance by considering interactions among features (Arbabshirani et al. 2017).

In order to find the optimal number of features to be retained, we gradually increase the number of features to be retained in feature selection from 1 to maximum, and use the SVM-based classifier for evaluation. When the ratio of the training set to the test set is 4:1, the relationship between the number of features to be retained and the model classification accuracy is shown in Fig. 1. We find that the increase in classification accuracy with the number of retained features roughly reflects the trend of first increase and then decrease. When the number of features to be retained increases from 1 to 80, the classification accuracy continues to increase; when the number of features to be retained is between 80 and 140, the classification accuracy rate fluctuates little and the classification accuracy rate reached the maximum while retaining 80 features; when the number of features to be retained exceeds 140, the classification accuracy of the model gradually decreases. Therefore, the optimal number of features to be retained is 80 to 140, and it is also considered that an increase in the number of features to be retained will lead to a longer training time of the model. Taking into account the accuracy of the model and the length of model training, it is optimal when the number of features to be retained is 80.

We chose the linear kernel based C-SVM (Cortes and Vapnik 1995) as the classifier. When the data from the two groups are not linearly separable, the C-SVM allows some training observations to be either misclassified or fall in the SVM margin through the use of slack variables ε_i with associated penalty parameter C.

$$\min \frac{1}{2} \| w \|^2 + C \sum_{i=1}^{N} \varepsilon_i \#$$

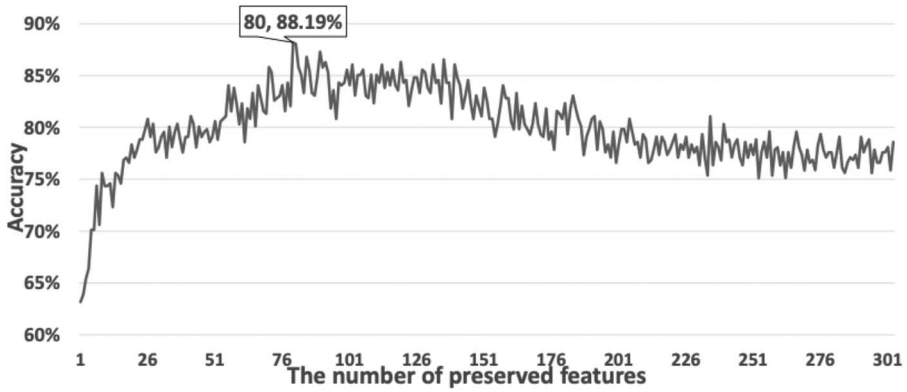

Fig. 1. Relationship between the number of preserved features and classification accuracy. The optimal number of features to be retained is 80, with an accuracy of 88.19%.

In the SVM experiment, the penalty parameter (also known as the slack variable) C was determined through a logarithmically spaced grid search, employing a geometric progression with a base of 2. The range of C values spanned from 2^{-15} to 2^{2}, with 20 equidistant points sampled along this logarithmic scale. This search was designed to identify the optimal C value, managing the trade-off between the margin and the size of the slack variables in the experiment. The specific C value selected from this logarithmic grid represents the parameter choice that yielded the best performance on the training data among the 20 sampled points. Here, the C selected from the grid search is 0.0968 for NMDARE versus HC model and 0.1800 for NMDARE versus VE model. The 80 feature subsets selected by the feature engineering of SVM-RFE were used as the input of the classifier. The samples were randomly divided into training set and validation set, with a ratio of 4:1. The validation set was used to test the current training accuracy after each training. The validation set should be mutually exclusive with the training set, that is, the validation samples do not appear in the training set. This was performed with functions from sklearn SVC (kernel = "linear") and RFECV (step = 10, cv = KFold [n_splits = 120, min_features_to_select = 10]), which implement a leave-one-out cross-validation allowing the estimation of the classifier accuracy at each step of the recursive ortho group elimination. Fivefold cross-validation was applied and the subsampling and cross-validation process was repeated 10 times. The C-SVM algorithm assigns a weight (a measure of feature strength that informs group membership) to each feature. The algorithm was run 50 times, and the resulting weight vectors were averaged to define a mean weight vector descriptive of the whole cohort.

We further explored the most discriminative brain regions and lobes between NMDARE patients and HCs based on the weights and anatomical location of features selected by NMDARE versus HCs model. The most discriminative brain regions and lobes between NMDARE and VE patients were also explored based on the weights and anatomical location of features selected by NMDARE versus VE model. By freesurfer, four features (cortical thickness, surface area, volume, and mean curvature) were automatically extracted for one cortical region. Every selected feature was assigned a weight by the C-SVM algorithm. The discriminating ability of a certain brain region was determined by its cumulative weights, sum of weights of all selected features located in that brain region. Similarly, the discriminating ability of a certain brain lobe was determined by its cumulative weights, sum of weights of all selected features located in that brain lobe. Weights of features that were located at the junction of two lobes were equally divided, and then summed into the calculations of both lobes. Brain lobes were the frontal lobe, temporal lobe, limbic system, parietal lobe and occipital lobe. A revised limbic system definition was adopted in our work; thus, the hippocampus, parahippocampal gyrus, amygdala, cingulate gyrus, insular cortex, orbitofrontal cortex, and corpus callosum were included (Catani et al. 2013; Pessoa and Hof 2015; Torrico and Abdijadid 2020).

Classification

SVM showed good overall performance, such as effectively avoiding overfitting and accommodating large feature spaces despite a small sample size and is by far the most utilized machine-learning classification in the field of neuroimaging.(Orrù et al. 2012; Arbabshirani et al. 2017; Yassin et al. 2020) Considering our limited number of samples, we used fivefold cross-validation strategy to estimate the generalization ability of our classification. The classifiers' performances were assessed by computing the sensitivity, specificity, precision, overall accuracy and F1 score based on the results of cross-validation in completely new validation set. We also implemented receiver operating characteristic (ROC) curves in these subjects, from which the area under the curve (AUC) was computed.

Statistical analysis

After confirming the normality of the distribution of the data (Lilliefors test), the data were represented as the mean ± SD (range) or median (interquartile range) (range). We used Mann–Whitney U- tests or Student's t-test for continuous variables and chi-squared test or Fisher's exact probability test for categorical variables. All demographic variables and selected discriminating features between NMDARE patients and HCs, and between NMDARE and VE patients were compared. Regarding the performance of the machine-learning models, the findings of each predictive output were classified as a true positive (TP), true negative (TN), false positive (FP), or false negative (FN). Accuracy was defined as the proportion of participants with correct prediction labels. Sensitivity was calculated as TP/(TP + FN), and specificity was calculated as TN/(TN + FP).

Results

A total of 109 sMRI-negative NMDARE patients in the acute phase, 108 HCs and 84 acute VE cases with negative MRI scans were included in the training phase. 29 NMDARE patients, 28 HCs and 26 VE cases were used to validate the models; they were completely new and not used at the time of training.

Table 2. Demographic characteristics of the cohorts of NMDARE patients, VE patients and healthy controls.

Characteristics	NMDARE and VE dataset			NMDARE and HCs dataset		
	NMDARE	VE	*P value*	NMDARE	HCs	*P value*
Number (n)	109	84	…	109	108	…
Age, Median (Q1 to Q3)	26.0 (19.0 to 33.0)	26.0 (19.0 to 37.2)	0.998	26.0 (19.0 to 33.0)	27.0 (19.0 to 38.0)	0.456
10 to 15 y, n (%)	9 (8.3%)	7 (8.3%)	…	9 (8.3%)	8 (7.4%)	…
16 to 20 y, n (%)	26 (23.9%)	20 (23.8%)	…	26(23.9%)	24 (22.2%)	…
21 to 25 y, n (%)	19 (17.4%)	14 (16.7%)	…	19 (17.4%)	19 (17.6%)	…
26 to 30 y, n (%)	21 (19.3%)	17 (20.2%)	…	21 (19.3%)	23 (21.3%0)	…
31 to 35 y, n (%)	7 (6.4%)	5 (6.0%)	…	7 (6.4%)	8 (7.4%)	…
36 to 40 y, n (%)	10 (9.2%)	8 (9.5%)	…	10 (9.2%)	9 (8.3%)	…
41–45 y, n (%)	4 (3.7%)	3 (3.6%)	…	4 (3.7%)	4(3.7%)	…
46 to 50 y, n (%)	5 (4.6%)	4 (4.8%)	…	5 (4.6%)	5 (4.6%)	…
51 to 55 y, n (%)	3 (2.8%)	2 (2.4%)	…	3 (2.8%)	3 (2.8%)	…
56 to 60 y, n (%)	1 (0.9%)	1 (1.2%)	…	1(0.9%)	1 (0.9%)	…
61 to 65 y, n (%)	3 (2.7%)	2 (2.4%)	…	3 (2.7%)	3 (2.8%)	…
80 to 85 y, n (%)	1 (0.9%)	1 (1.2%)	…	1 (0.9%)	1 (0.9%)	…
Sex (N, %)						
Female	63 (57.8%)	46 (54.8%)	0.520	63 (57.8%)	76 (70.3%)	0.069
Male	46 (42.2%)	38 (45.2%)		46 (42.2%)	32 (29.7%)	
Seizure	71 (65.14%)	54 (64.29%)	0.902	71 (65.14%)	…	…
Mental and behavior disorder	93 (85.32%)	65 (77.38%)	0.156	93 (85.32%)	…	…
Unconscious	50 (46.30%)	19 (22.62%)	<0.001	50 (46.30%)	…	…
ICU admission	9 (8.26%)	0 (0.00%)	0.007	9 (8.26%)	…	…
CSF pleocytosis	55 (50.46%)	21 (25.00%)	<0.001	55 (50.46%)	…	…
CSF elevated protein	37 (33.94%)	33 (39.29%)	0.444	37 (33.94%)	…	…
Abnormal electroencephalography	64 (77.11%)	59 (70.24%)	0.314	64 (77.11%)	…	…

NMDAR, N-methyl-D-aspartate receptor; VE, viral encephalitis; HCs, Health controls; ICU, Intensive Care Unit; CSF, Cerebrospinal Fluid.

Table 3. Performances of NMDARE versus HCs classifier and NMDARE versus VE classifier for fivefold cross-validation.

Fold	NMDARE versus HCs model				NMDARE versus VE model			
	SE	SP	ACC	AUC	SE	SP	ACC	AUC
1	0.9479	0.9673	0.9572	0.9913	0.8762	0.8434	0.8609	0.9386
2	0.9389	0.9714	0.9545	0.9916	0.8845	0.8365	0.8651	0.9353
3	0.923	0.9616	0.942	0.989	0.8585	0.8075	0.8359	0.9158
4	0.9243	0.9552	0.9387	0.9855	0.8861	0.8259	0.8594	0.9292
5	0.9381	0.9668	0.9526	0.9907	0.8697	0.8269	0.849	0.9245
Mean	0.9344	0.9644	0.949	0.9896	0.875	0.828	0.8541	0.9287
SD	0.0001	0.0001	0.0001	0.0001	0.0001	0.0002	0.0001	0.0001

NMDAR, N-methyl-D-aspartate receptor; VE, viral encephalitis; HCs, health controls; SE, sensitivity; SP, specificity; ACC, accuracy; AUC, area under the receiver operating characteristic curve; SD, standard deviation.

Demographics and clinical information

The ages ranged from 12 to 85 years old for 109 NMDARE patients (median (Q1-Q3): 26.0 (19.0-33.0)), 13 to 84 years old for VE patients (median (Q1-Q3): 26.0 (19.0-37.2)) and 10–85 years old for HCs (median (Q1-Q3): 27.0 (19.0-38.0)). Individuals in the patient and control groups were of mixed sex (63 females/46 males in NMDARE group, 46 females/38 males in VE group, 76 females/32 males in HC group). There were no significant differences between NMDARE group and HCs group, and between NMDARE group and VE group with regard to age ($P = 0.456$, 0.998, respectively) and sex distribution ($P = 0.069$, 0.520, respectively). Demographics information are summarized in Table 2.

Performance of the classifiers

In training set, the average AUC based on the 5-fold cross-validation for NMDARE versus HCs model was 0.9896. And for NMDARE versus VE model the value was 0.9287. The detail performances of NMDARE versus HCs classifier and NMDARE versus VE classifier for fivefold cross-validation are shown in Table 3.

In completely new validate set, the performance of NMDARE and HCs classification reached 93.0% accuracy, 86.2% sensitivity, 100% specificity, and 100% precision (Fig. 2A). The AUC of the ROC curve was 0.963 (Fig. 2B). And for the performance of NMDARE and VE classification reached 78.2% accuracy, 79.3% sensitivity, 76.9% specificity, and 79.3% precision (Fig. 2C). The AUC of the ROC curve was 0.879 (Fig. 2D).

Weights and distribution of the 80 selected features for discriminations

The weights and locating lobes of the 80 discriminative features between NMDARE and HCs are shown in Supplementary Table 2. After categorizing them into regions, 63 cortex regions in either the right or left hemisphere and 5 subcortical structures were obtained (Fig. 3A). The top 10 discriminative regions (ranking by cumulative weight) for NMDARE and HCs classification were the right posterior-ventral part of the cingulate gyrus (vPCC, isthmus of the cingulate gyrus) (cumulative weight = 0.494), left superior frontal sulcus (cumulative weight = 0.426), left paracentral lobule and sulcus (cumulative weight = 0.405), right temporal pole

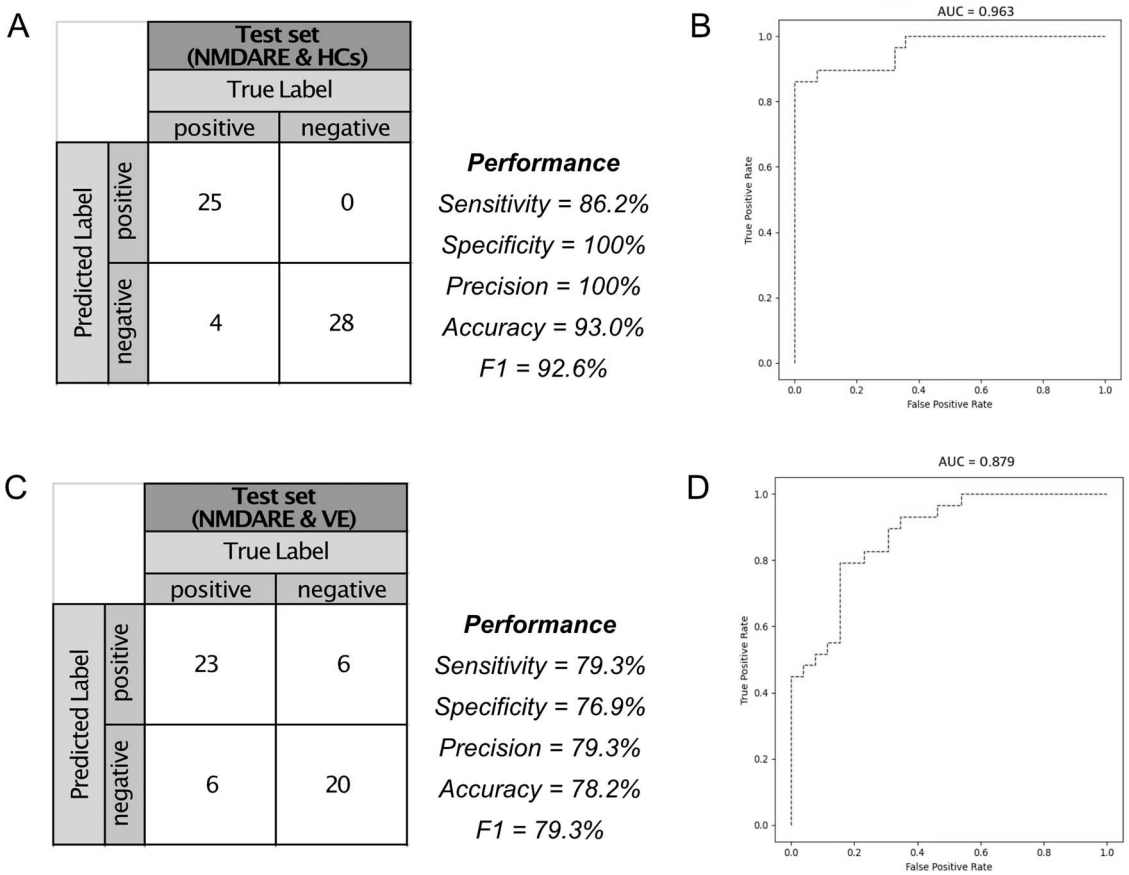

Fig. 2. Performance of classifications in new validation sets. A) The performance (measured by sensitivity, specificity, precision, accuracy and F1 score) and confusion matrix of support vector machine classification in NMDARE and HCs. B) Receiver operating characteristic (ROC) curve of the performance: The area under the curve (AUC) was 0.963. C) The performance (measured by sensitivity, specificity, precision, accuracy and F1 score) and confusion matrix of support vector machine classification in NMDARE and VE. (D) Receiver operating characteristic (ROC) curve of the performance: The area under the curve (AUC) was 0.879. *NMDARE, anti-N-methyl-D-aspartate receptor encephalitis; HCs, healthy controls; VE, viral encephalitis.*

(cumulative weight = 0.405), right superior parietal lobule (lateral part of P1) (cumulative weight = 0.401), right middle occipital gyrus (O2, lateral occipital gyrus) (cumulative weight = 0.351), right orbital sulci (H-shaped sulci) (cumulative weight = 0.346), left precuneus (medial part of P1) (cumulative weight = 0.341), left fronto-marginal gyrus (of Wernicke) (cumulative weight = 0.340), and sulcus and right short insular gyri (cumulative weight = 0.338) (Fig. 3B). Important features for classification were predominately present in the frontal lobe (cumulative weight = 4.3725, contribution rate of 29.86%), second in the temporal lobe (cumulative weight = 2.573, contribution rate of 17.57%), third in the occipital lobe (cumulative weight = 2.546, contribution rate of 17.39%), then in the limbic lobe (cumulative weights = 2.299, contribution rate of 15.70%), the parietal lobe (cumulative weights = 1.9525, contribution rate of 13.33%), and last in the subcortical structure (cumulative weight = 0.899, contribution rate of 6.14%). The cumulative weights of the five lobes and subcortical structure are shown in Fig. 4.

As for discriminative features of NMDARE and VE (their weights and locating lobes are shown in Supplementary Table 3), 62 cortex regions in either the right or left hemisphere and 5 subcortical structures were obtained (Fig. 5A). The top 10 discriminative regions (ranking by cumulative weight) for NMDARE and VE classification were the right posterior ramus (or segment) of the lateral sulcus (or fissure) (cumulative weight = 0.794), left orbital part of the inferior frontal gyrus (cumulative weight = 0.779), left marginal branch (or part) of the cingulate sulcus (cumulative weight = 0.698), left pericallosal sulcus (S of corpus callosum) (cumulative weight = 0.624), left lateral occipito-temporal gyrus (fusiform gyrus, O4-T4) (cumulative weight = 0.615), right short insular gyri (cumulative weight = 0.596), posterior corpus callosum (cumulative weight = 0.568), left transverse frontopolar gyri and sulci (medial part of P1) (cumulative weight = 0.557), right orbital sulci (H-shaped sulci) (cumulative weight = 0.554), and left precentral gyrus (cumulative weight = 0.504) (Fig. 5B). Important features for classification were predominately present in the frontal lobe (cumulative weight = 7.679, contribution rate of 33.55%), second in the limbic lobe (cumulative weight = 5.126, contribution rate of 22.40%), third in the temporal lobe (cumulative weights = 4.2285, contribution rate of 18.48%), then in the occipital lobe (cumulative weight = 2.2235, contribution rate of 9.72%) and in the subcortical structure (cumulative weight = 1.54, contribution rate of 6.73%), last in the parietal lobe (cumulative weight = 1.535, contribution rate of 6.71%). The cumulative weights of the five lobes and subcortical structure are shown in Fig. 6.

Quantitative analysis of 80 discriminative features between NMDARE patients and HCs and VE patients

In the quantitative analysis of the discriminative features between NMDARE patients and HCs, NMDARE patients presented with significantly lower thickness, area, and volume and higher mean curvature. For the 13 regions with discriminative area

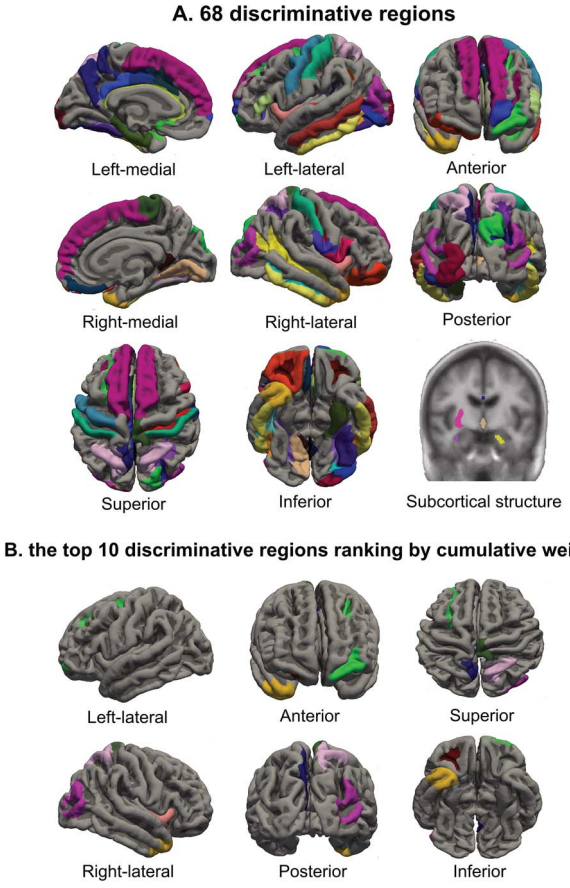

Fig. 3. Visualization of discriminative regions of NMDARE and HCs and the top 10 discriminative regions ranking by cumulative weights. A) Sixty-three cortex regions and 5 subcortical structures whose features were selected by classification. B) The top 10 discriminative regions ranking by cumulative weights mainly involved front lobe, medial temporal lobe, and limbic lobe.

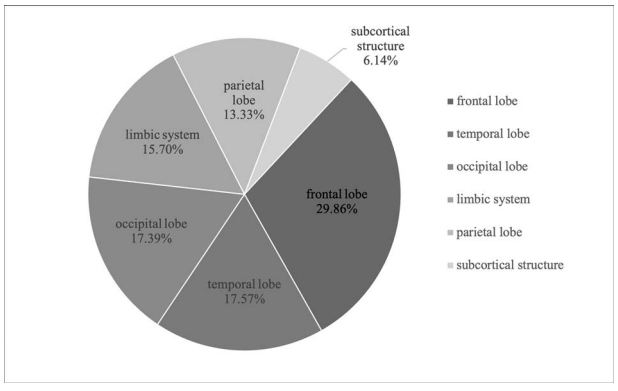

Fig. 4. Distribution of the 80 selected features for discriminating NMDARE from HCs. Important features for classifier were predominately present in the frontal lobe (cumulative weight = 4.3725, contribution rate of 29.86%), second in the temporal lobe (cumulative weight = 2.573, contribution rate of 17.57%), third in the occipital lobe (cumulative weight = 2.546, contribution rate of 17.39%), then in the limbic lobe (cumulative weights = 2.299, contribution rate of 15.70%), the parietal lobe (cumulative weights = 1.9525, contribution rate of 13.33%), and last in the subcortical structure (cumulative weight = 0.899, contribution rate of 6.14%).

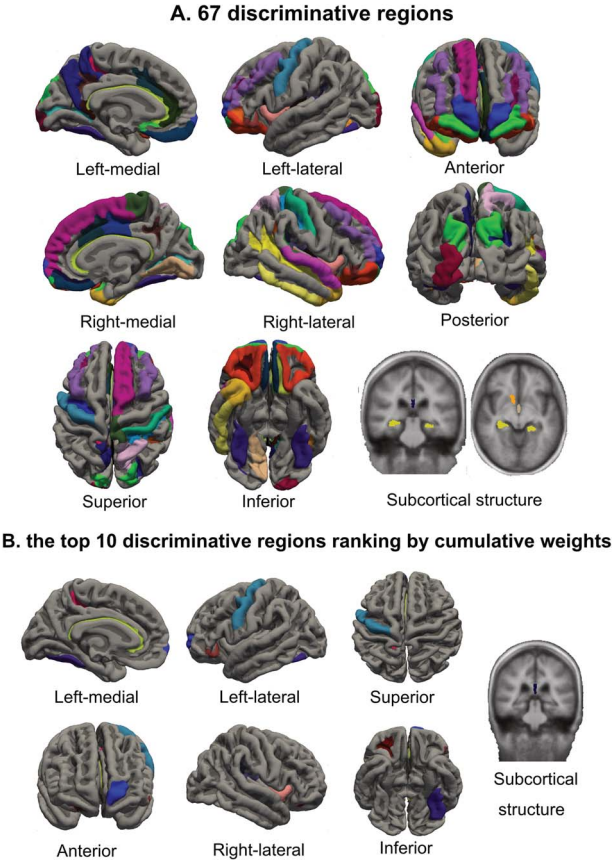

Fig. 5. Visualization of discriminative regions of NMDARE and VE and the top 10 discriminative regions ranking by cumulative weights. A) 62 cortex regions and 5 subcortical structures whose features were selected by classification. B) The top 10 discriminative regions ranking by cumulative weights mainly involved front lobe and limbic system.

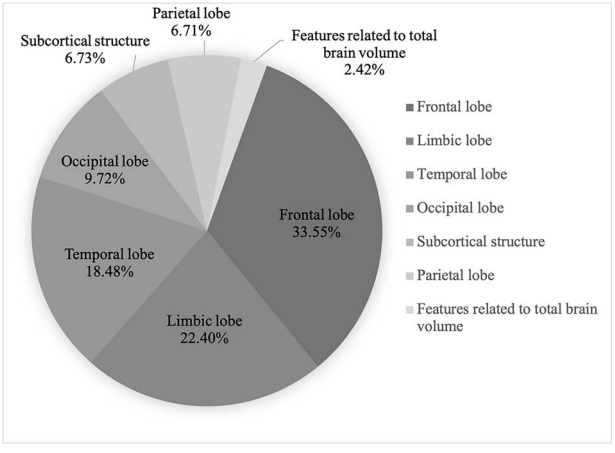

Fig. 6. Distribution of the 80 selected features for discriminating NMDARE from VE. Important features for classification were predominately present in the frontal lobe (cumulative weight = 7.679, contribution rate of 33.55%), second in the limbic system (cumulative weight = 5.126, contribution rate of 22.40%), third in the temporal lobe (cumulative weights = 4.2285, contribution rate of 18.48%), then in the occipital lobe (cumulative weight = 2.2235, contribution rate of 9.72%) and in the subcortical structure (cumulative weight = 1.54, contribution rate of 6.73%), last in the parietal lobe (cumulative weight = 1.535, contribution rate of 6.71%). The weight of volume of all voxels without ventricles is 0.555, contribution rate of 2.42%.

features, the area in the patient group compared with the HC group was decreased in all 13 regions, and significance was observed in 8 of these regions, such as posterior-dorsal part of the cingulate gyrus and middle-posterior part of the cingulate gyrus and sulcus of left hemisphere (Student's t-test, $P < 0.05$; Fig. 7A). In 23 regions with discriminative thickness features, decreased thickness was observed in 21 regions when comparing NMDARE

patients and HCs, and 18 of these regions were significant after Student's t-test, such as temporal pole and short insular gyri of right hemisphere ($P < 0.05$; Fig. 7B). Additionally, compared with the HC group, the group of NMDARE patients showed smaller volumes in 11 out of 18 regions, and 8 of these regions were significant according to Student's t-test, such as posterior ramus (or segment) of the lateral sulcus (or fissure) and lateral occipitotemporal gyrus (fusiform gyrus, O4-T4) of left hemisphere ($P < 0.05$; Fig. 7C). Mean curvature is a feature that measures the sharpness of sulci and gyri. It has been proven to increase with cortical thinning and reductions in gray matter normalization in anorexia nervosa patients during weight restoration (Bernardoni et al. 2018). In our study, 14 out of 26 mean curvature features were increased in the patient group compared with the HC group, and 7 of them were significant, such as short insular gyri of left hemisphere and anterior transverse collateral sulcus of right hemisphere (Student's t-test, $P < 0.05$; Fig. 7D).

But in the quantitative analysis of the discriminative features between NMDARE patients and VE patients, only 8 of 80 features were significant between two groups (Fig. 8). No specific pattern was found for NMDARE patients, comparing to VE patients.

In short, the distribution and quantitative analysis of these discriminative features revealed that NMDARE patients experience a pattern of widespread cerebral cortex atrophy even in the early stages. But comparing to VE patients, no specific pattern was found for NMDARE patients.

Discussion

Using machine learning with MRI data, we identified the most discriminative structural features of NMDARE patients at an early stage. After classification, their accuracy and sensitivity reached 93.0% and 86.2%, respectively, which suggested that these discriminative structural features extracted from classification could be potential imaging biomarkers of this disease.

Analysis of these discriminative features revealed that widespread atrophy of the cerebral cortex is the characteristic pattern of structural alterations in anti-NMDA receptor encephalitis at an early stage. This is consistent with patients' highly variable symptoms and may help to explain the clinico-radiological paradox, the condition of NMDARE patients is severe but less patients show abnormality on conventional MRI, in NMDARE. The presence of brain atrophy on autopsy in anti-NMDAR patients who died 4 months after symptom onset (Tüzün et al. 2009) and reversible diffuse cerebral atrophy (DCA) on patient MRI, which developed within 14 days after symptom onset at the earliest (Kataoka et al. 2017) and progressed over the course of 1 to 7 years (Iizuka et al. 2010; Taguchi et al. 2011; Iizuka et al. 2016), may be the most important evidence. Further microscopic autopsy studies of patients revealed remarkable loss of pyramidal neurons in the hippocampus and neuronal degeneration in the neocortex (Tüzün et al. 2009). Additionally, our MRI findings have notable parallels with those obtained in ketamine (NMDAR antagonist) users (Wang et al. 2013), where diffuse damage and atrophy of the brain was observed after ketamine addicts of 0.5 to 12 years.

It is controversial whether NMDARE itself contributes to DCA. Some researchers have speculated that potential risk factors, including malnutrition, systemic complications, status epilepticus, prolonged use of corticosteroids, long-term exposure to various antiepileptic agents, and prolonged use of propofol, may be involved in DCA (Iizuka et al. 2010; Iizuka et al. 2016). However, in our study, all NMDARE patients, including patients with no systemic complications, showed potential DCA. This indicated that neuronal impairments are caused by special NMDAR antigen–antibody reactions occurring in the early stages even in those patients without serious conditions. This direct role of the antibodies in brain atrophy was also confirmed in a mouse model of anti-NMDA receptor encephalitis. In Westbrook's recent study, they used active immunization of immune competent mice with conformationally stabilized, native-like NMDA receptors, which successfully induced fulminant encephalitis. Patchy areas of cell death were observed in brain sections in the histological analysis at 6 weeks postimmunization (Jones et al. 2019). Therefore, we hypothesize that similar to NMDA antagonists (Newcomer et al. 2000; Wang et al. 2013), continuous administration of anti-NMDA antibodies for several months induces a prolonged NMDA receptor state of hypofunction that causes neuronal death in many cerebral cortical and limbic brain regions, resulting in widespread cerebral cortex atrophy.

In our study, although important features for discriminating were present in all five major lobes, the frontal and temporal lobes had significantly high cumulative weights, suggesting that the most important structural changes occurred in these lobes. This is consistent with many sMRI studies (case studies and case series report clear volume reductions in frontal cortical regions and hippocampal area after a follow-up 9 months to 1 year) (Finke et al. 2016; Phillips et al. 2018; Laurikainen et al. 2019), several functional MRI (fMRI) studies (all studies identified frontoparietal, frontotemporal and hippocampal connection disrupted in a cohort of patients, which proved to be reliably discriminative features between patients and controls in Peer's study, yielding an overall accuracy of 81%) (Finke et al. 2013; Peer et al. 2017; Phillips et al. 2018), and a positron emission tomography (PET)/computed tomography (CT) study (a case report that showed bilateral hypermetabolism in insular and prefrontal cortex during the acute phase) (Hegen et al. 2016) of NMDARE patients. This is in line with NMDARs being widespread in the CNS (Paoletti et al. 2013) and predominantly found in the forebrain and limbic system, most notably the hippocampal area (Dalmau et al. 2008; Iizuka et al. 2008; Tüzün et al. 2009). Therefore, these lobes should be given more attention in clinical work to identify patients.

There were 10 important regions (calculated by cumulative weights) that contributed to the discrimination of the identified NMDARE patients from HCs in our study. Considering the usually unremarkable structural MRI findings in NMDARE, the importance of these selected regions has been mostly supported by the results of advanced imaging analyses (fMRI, PET-CT) of NMDARE patients and studies of NMDA antagonists (such as ketamine). In a recent resting-state (rs)-fMRI study by Cai et al. (2020), NMDARE patients showed decreased amplitude of low-frequency fluctuations values in the bilateral PCC and left precuneus in brain functional activity analyses. Significantly increased FC between the bilateral PCC and several other regions has been observed. Furthermore, in Hegen's MRI and PET-CT study of a patient, brain MRI abnormalities were found in both insular cortices, whereas F18-FDG-PET showed hypermetabolism during the acute phase (Hegen et al. 2016). Nagels et al. conducted an fMRI study using the NMDA antagonist ketamine in healthy human subjects while they freely spoke about Thematic Apperception Test pictures. The group treated with S-ketamine showed lower blood oxygen level-dependent signals in the right hemispheric inferior and middle temporal gyri than the placebo control group. This finding was consistent with the results from ROI analyses with both hemispheres and the whole brain (Nagels et al. 2018). These results also

A

	Brain area	thickness t	thickness sig
Frontal lobe	Right Subcentral gyrus (central operculum) and sulci	-4.825	<0.001
	Left Fronto-marginal gyrus (of Wernicke) and sulcus	-4.523	<0.001
	Right Horizontal ramus of the anterior segment of the lateral sulcus (or fissure)	-4.195	<0.001
	Right Orbital sulci (H-shaped sulci)	-3.248	0.001
	Left Superior frontal sulcus	0.872	0.384
Temporal lobe	Right Superior temporal sulcus (parallel sulcus)	-7.558	<0.001
	Right Inferior temporal sulcus	-7.367	<0.001
	Right Temporal pole	-4.674	<0.001
	Left Medial occipito-temporal sulcus (collateral sulcus) and lingual sulcus	-4.016	<0.001
	Left Planum polare of the superior temporal gyrus	-1.033	0.303
	Left Transverse temporal sulcus	-0.008	0.994
Limbic system	Right Short insular gyri	-6.614	<0.001
	Left Parahippocampal gyrus, parahippocampal part of the medial occipito-temporal gyrus, (T5)	-5.703	<0.001
	Left Subcallosal area, subcallosal gyrus	-4.034	<0.001
Occipital lobe	Right Middle occipital gyrus (O2, lateral occipital gyrus)	-7.42	<0.001
	Left Inferior occipital gyrus (O3) and sulcus	-4.735	<0.001
	Right Superior occipital sulcus and transverse occipital sulcus	-4.161	<0.001
	Right Lateral occipito-temporal sulcus	-4.025	<0.001
	Left Lateral occipito-temporal sulcus	-3.513	0.001
	Left Occipital pole	-1.842	0.067
Parietal lobe	Left Sulcus intermedius primus (of Jensen)	-4.776	<0.001
	Left Precuneus (medial part of P1)	-3.513	0.001
	Left Superior parietal lobule (lateral part of P1)	0.941	0.348

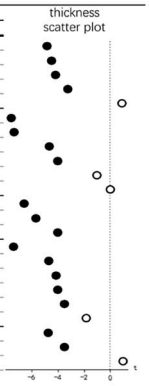

B

	Brain area	surface area t	surface area sig
Frontal lobe	Right Precentral gyrus	-4.8	<0.001
	Right Paracentral lobule and sulcus	-4.127	<0.001
	Left Triangular part of the inferior frontal gyrus	-3.355	0.001
	Right Orbital part of the inferior frontal gyrus	-1.967	0.05
	Right Vertical ramus of the anterior segment of the lateral sulcus (or fissure)	-1.016	0.311
	Left Transverse frontopolar gyri and sulci	-0.779	0.437
	Left Superior frontal sulcus	-0.6	0.549
Temporal lobe	Left Middle temporal gyrus	-3.296	0.001
Limbic system	Left Posterior-dorsal part of the cingulate gyrus (dPCC)	-5.34	<0.001
	Left Middle-posterior part of the cingulate gyrus and sulcus (pMCC)	-5.175	<0.001
	Right Posterior-ventral part of the cingulate gyrus (vPCC, isthmus of the cingulate gyrus)	-2.747	0.007
	Right Inferior segment of the circular sulcus of the insula	-0.222	0.825
Occipital lobe	Left Posterior transverse collateral sulcus	-0.179	0.858

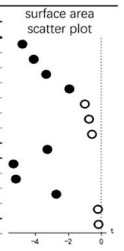

C

	Brain area	volume t	volume sig
Frontal lobe	Left Vertical ramus of the anterior segment of the lateral sulcus (or fissure)	-2.159	0.032
	Left Horizontal ramus of the anterior segment of the lateral sulcus (or fissure)	-1.853	0.065
	Right Central sulcus (Rolando's fissure)	-1.313	0.191
	Right Orbital sulci (H-shaped sulci)	0.796	0.427
Temporal lobe	Left Lateral occipito-temporal gyrus (fusiform gyrus, O4-T4)	-3.748	<0.001
	Left Posterior ramus (or segment) of the lateral sulcus (or fissure)	-3.219	0.002
Limbic system	Right Orbital gyri	-2.453	0.015
Occipital lobe	Left Inferior occipital gyrus (O3) and sulcus	-4.594	<0.001
	Right Superior occipital gyrus (O1)	-4.343	<0.001
	Left Anterior occipital sulcus and preoccipital notch (temporo-occipital incisure)	-2.702	0.007
	Right Lateral occipito-temporal sulcus	0.545	0.586
Parietal lobe	Left Precuneus (medial part of P1)	-3.986	<0.001
	Right Superior parietal lobule (lateral part of P1)	-1.346	0.18
Subcortical structure	CC_Central	0.902	0.369
	Right-Inf-Lat-Vent	1.628	0.106
	Right-Putamen	1.801	0.073
	Left-Hippocampus	2.224	0.027
	3rd-Ventricle	2.723	0.007

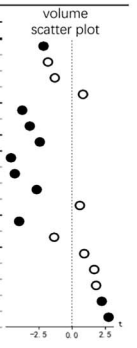

D

	Brain area	meancurv t	meancurv sig
Frontal lobe	Right Straight gyrus, Gyrus rectus	-2.812	0.005
	Right Opercular part of the inferior frontal gyrus	-0.751	0.454
	Left Superior frontal gyrus (F1)	-0.628	0.531
	Right Superior frontal gyrus (F1)	-0.305	0.761
	Left Orbital sulci (H-shaped sulci)	0.166	0.868
	Left Middle frontal sulcus	1.324	0.187
	Left Precentral gyrus	1.579	0.116
	Left Horizontal ramus of the anterior segment of the lateral sulcus (or fissure)	2.206	0.029
Temporal lobe	Left Inferior temporal gyrus	-2.848	0.005
	Right Medial occipito-temporal sulcus (collateral sulcus) and lingual sulcus	-1.003	0.317
	Right Inferior temporal gyrus	-0.837	0.404
	Right Temporal pole	1.836	0.068
	Right Anterior transverse collateral sulcus	2.061	0.041
Limbic system	Left Pericallosal sulcus (S of corpus callosum)	-2.153	0.033
	Right Posterior-ventral part of the cingulate gyrus (vPCC, isthmus of the cingulate gyrus)	-0.316	0.752
	Left Middle-anterior part of the cingulate gyrus and sulcus (aMCC)	0.973	0.332
	Left Short insular gyri	5.306	<0.001
Occipital lobe	Left Middle occipital gyrus (O2, lateral occipital gyrus)	-4.153	<0.001
	Right Middle occipital gyrus (O2, lateral occipital gyrus)	-2.418	0.017
	Right Lingual gyrus, ligual part of the medial occipito-temporal gyrus, (O5)	2.099	0.037
	Right Lateral occipito-temporal sulcus	2.194	0.029
Parietal lobe	Left Precuneus (medial part of P1)	-1.028	0.305
	Right Superior parietal lobule (lateral part of P1)	0.858	0.392
	Left Postcentral gyrus	1	0.318
	Right Postcentral gyrus	2.051	0.042
	Right Intraparietal sulcus (interparietal sulcus) and transverse parietal sulci	2.684	0.008

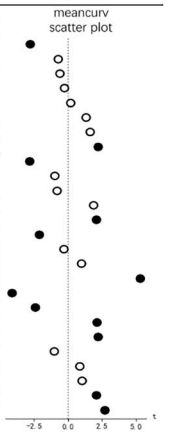

Fig. 7. Quantitative analysis of 80 discriminative features NMDARE patients and HCs. A) Comparison of 13 discriminative area features between NMDARE patients and HCs: The area in the patient group was lower in 13 regions than in the HCs group, and significance was observed in 8 of these regions (Student's t-test, $P < 0.05$). B) Comparison of 23 discriminative thickness features between NMDARE patients and HCs: Decreased thickness was observed in 23 regions, and 18 of these regions were significant after Student's t-tests ($P < 0.05$). C) Comparison of 19 discriminative volume features between NMDARE patients and healthy controls: NMDARE patients showed smaller volumes in 11 out of 18 regions, and 8 of these regions were significant according to Student's t-tests ($P < 0.05$). D) Comparison of 26 discriminative mean curvature features between NMDARE patients and healthy controls: 14 out of 26 mean curvature features were increased in the patient group compared with the HC group, and 7 of them were significant (Student's t-test, $P < 0.05$).

A

	Brain area	thickness t	thickness sig
Frontal lobe	Right Middle frontal gyrus (F2)	-0.159	0.874
	Right Superior part of the precentral sulcus	0.216	0.829
	Left Lateral orbital sulcus	0.293	0.77
	Left Fronto-marginal gyrus (of Wernicke) and sulcus	1.395	0.165
	Left Superior part of the precentral sulcus	2.039	0.043
	Left Precentral gyrus	2.2	0.029
Temporal lobe	Right Temporal pole	-0.416	0.678
	Right Lateral aspect of the superior temporal gyrus	0.753	0.453
	Right Superior temporal sulcus (parallel sulcus)	0.967	0.335
	Right Transverse temporal sulcus	1.48	0.141
	Right Planum temporale or temporal plane of the superior temporal gyrus	1.979	0.049
Limbic system	Right Orbital gyri	-1.699	0.091
	Left Orbital gyri	-0.457	0.648
	Left Short insular gyri	0.916	0.361
Occipital lobe	Left Calcarine sulcus	0.179	0.858
	Left Occipital pole	0.538	0.591
Parietal lobe	Right Sulcus intermedius primus (of Jensen)	1.268	0.207

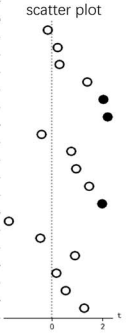

B

	Brain area	surface area t	surface area sig
Frontal lobe	Left Vertical ramus of the anterior segment of the lateral sulcus (or fissure)	-1.908	0.058
	Right Transverse frontopolar gyri and sulci	-0.708	0.48
	Left Transverse frontopolar gyri and sulci	0	1
	Left Orbital part of the inferior frontal gyrus	1.585	0.115
Temporal lobe	Right Posterior ramus (or segment) of the lateral sulcus (or fissure)	-2.316	0.022
	Left Posterior ramus (or segment) of the lateral sulcus (or fissure)	-1.556	0.121
	Right Planum polare of the superior temporal gyrus	0.324	0.746
Limbic system	Right Middle-anterior part of the cingulate gyrus and sulcus (aMCC)	-1.741	0.083
	Left Middle-anterior part of the cingulate gyrus and sulcus (aMCC)	-1.507	0.133
	Left Anterior part of the cingulate gyrus and sulcus (ACC)	-1.083	0.28
	Left Marginal branch (or part) of the cingulate sulcus	-0.674	0.501
	Right Long insular gyrus and central sulcus of the insula	-0.373	0.709
	Left Pericallosal sulcus (S of corpus callosum)	-0.035	0.972
Occipital lobe	Left Superior occipital gyrus (O1)	-0.431	0.667
	Left Lateral occipito-temporal sulcus	0.523	0.601
	Left Calcarine sulcus	0.829	0.408
Parietal lobe	Left Precuneus (medial part of P1)	-2.532	0.012
	Right Subparietal sulcus	-0.655	0.513

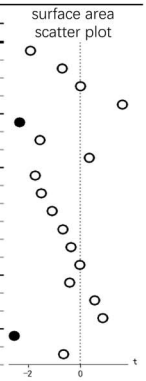

C

	Brain area	volume t	volume sig
Frontal lobe	Right Vertical ramus of the anterior segment of the lateral sulcus (or fissure)	-2.547	0.012
	Right Orbital sulci (H-shaped sulci)	-1.657	0.099
	Right Fronto-marginal gyrus (of Wernicke) and sulcus	-0.741	0.46
	Left Straight gyrus, Gyrus rectus	0.258	0.796
	Left Orbital part of the inferior frontal gyrus	1.217	0.225
Temporal lobe	Right Posterior ramus (or segment) of the lateral sulcus (or fissure)	-1.672	0.096
	Right Lateral occipito-temporal gyrus (fusiform gyrus, O4-T4)	-0.64	0.523
	Right Inferior temporal gyrus	-0.194	0.846
Limbic system	Right Orbital gyri	-1.858	0.065
	Right Pericallosal sulcus (S of corpus callosum)	-0.94	0.348
	Left Subcallosal area, subcallosal gyrus	0.536	0.592
	Right Short insular gyri	1.727	0.086
Occipital lobe	Right Calcarine sulcus	-0.654	0.514
	Left Superior occipital gyrus (O1)	0.187	0.852
Parietal lobe	Left Subparietal sulcus	-1.078	0.283
Subcortical structure	3rd-Ventricle	-1.864	0.064
	Left-Hippocampus	-1.788	0.075
	Right-Hippocampus	-1.159	0.248
	Right-Accumbens-area	-0.94	0.349
	CC_Posterior	1.056	0.293

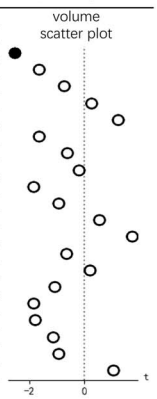

D

	Brain area	meancurv t	meancurv sig
Frontal lobe	Left Precentral gyrus	-0.594	0.553
	Left Orbital part of the inferior frontal gyrus	0.126	0.899
	Left Middle frontal gyrus (F2)	0.306	0.76
	Right Orbital part of the inferior frontal gyrus	0.53	0.597
	Right Orbital sulci (H-shaped sulci)	1.177	0.241
	Right Paracentral lobule and sulcus	1.3	0.196
	Right Superior frontal gyrus (F1)	1.556	0.121
	Left Transverse frontopolar gyri and sulci	1.636	0.103
	Right Straight gyrus, Gyrus rectus	1.74	0.083
	Left Medial orbital sulcus (olfactory sulcus)	1.881	0.061
	Right Suborbital sulcus (sulcus rostrales, supraorbital sulcus)	2.32	0.021
	Left Middle frontal sulcus	2.611	0.01
Temporal lobe	Right Temporal pole	1.458	0.146
	Left Lateral occipito-temporal gyrus (fusiform gyrus, O4-T4)	1.504	0.134
Limbic system	Left Long insular gyrus and central sulcus of the insula	-0.945	0.346
	Right Middle-posterior part of the cingulate gyrus and sulcus (pMCC)	-0.163	0.87
	Left Posterior-ventral part of the cingulate gyrus (vPCC, isthmus of the cingulate gyrus)	0.533	0.595
	Left Pericallosal sulcus (S of corpus callosum)	1.052	0.295
	Left Marginal branch (or part) of the cingulate sulcus	1.127	0.262
Occipital lobe	Right Superior occipital gyrus (O1)	-0.847	0.398
	Right Lingual gyrus, ligual part of the medial occipito-temporal gyrus, (O5)	0.993	0.322
	Right Superior occipital sulcus and transverse occipital sulcus	1.631	0.105
Parietal lobe	Right Postcentral gyrus	-0.92	0.359
	Right Superior parietal lobule (lateral part of P1)	0.455	0.65

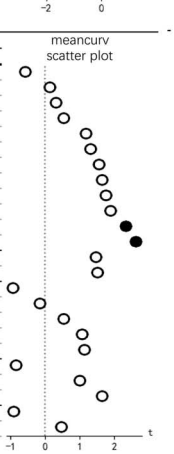

Fig. 8. Quantitative analysis of 80 discriminative features between NMDARE patients and VE patients. A) Comparison of discriminative area features between NMDARE patients and VE patients. B) Comparison of discriminative thickness features between NMDARE patients and VE patients. C) Comparison of discriminative volume features between NMDARE patients and VE patients. D) Comparison of discriminative mean curvature features between NMDARE patients and VE patients.

demonstrated an association between damaged brain regions and NMDARE symptom formation.

Since NMDARE and VE have similar manifestations, conventional CSF or blood tests during the early disease stages, it is often difficult to differentiate the two entities. Our model showed certain diagnostic power between NMDARE and VE, with AUC of 0.879 in new test set. This is comparable with previous studies. Xiang et al. (2022) proposed a deep-learning based model using features extracted from multi-sequence MRI (T1WI, T2WI, FLAIR, and DWI) in clinical protocol in 160 patients with autoimmune encephalitis, 177 herpes simplex virus encephalitis (HSVE) patients, and 184 HCs and validated in another 15 autoimmune encephalitis, 17 HSVE patients, and 20 HCs. Results demonstrated that the model had high diagnostic power, resulting in AUCs of 0.83 for autoimmune encephalitis and 0.88 for HSVE both in training and testing cohorts. Instead of only using the hippocampal regions as an input in their study, our study used whole brain features to include potentially valuable information as much as possible. Also, the features were segmented automatic in our study which may reduce the manual errors contained in manual segment. Maybe our model has more practical application values.

The accuracy of classification of NMDARE and VE was not that high (78.2%) in our new validation set, indicating this machine learning model was difficult to distinguish these two similar diseases accurately. However, it is suitable to serves as a screening tool for primary care hospitals. Since diagnosis NMDARE by antibody tests require hospitals to be equipped with specific instruments that are complex, costly and are not available in all primary care hospitals. And sending all suspicious NMDARE patients' blood/CSF samples to a remote test center is costly and time-consuming, which may delay valuable treatment time. Our automatic NMDAR detection model based on MRI in clinical protocol, has advantages as a noninvasive examination method and can be easily applied in primary hospital and cost less. Patients at high-risk of NMDARE identified by our model could be arranged further antibody confirm tests and implemented appropriate preventive measures, which may significantly improve the survival rate and prognosis of NMDARE. In further studies, we should also apply and combine clinical features, blood and CSF features to improve the model performance.

To our knowledge, this is the first study to reveal that widespread cerebral cortex atrophy is the characteristic pattern of structural alterations in NMDARE at an early stage. However, our study has several limitations. First, the scanner was either Trio or Skyla. There might be certain variability in image feature values calculated from MR images taken with different MR scanners. Further study to address the issue of scanner variability is needed. Second, there are other potential confounders which we have not accounted for, including educational attainment and ethnicity. Finally, these models have not undergone external validation. External validation set are needed to test the accuracy and reproducibility of the models.

Conclusions

Our research shows potential atrophy across the entire cerebral cortex at an early stage in NMDARE patients. Comparing to VE patients, no specific pattern was found.

Author contributions

Jinmei Li had full access to all of the data in the study and takes responsibility for the integrity of the data and the accuracy of the data analysis. Jinmei Li, Zhuoling Xiao (Resources, Conceptualization Methodology, Writing-review & editing), Sisi Shen, Ran Wei, Yu Gao, Xinyuan Yang, Guoning Zhang, Bo Yan (Investigation, Data curation, Formal Analysis, Software), Sisi Shen, Bo Yan (Writing-original draft), Jinmei Li (Funding acquisition, Supervision)

Supplementary material

Supplementary material is available at *Cerebral Cortex* online.

Funding

Science & Technology Department of Sichuan Province (No. 2019YFH0145) and National Natural Science Foundation of China (No. 81571272) to J.L.

Conflict of interest statement: None declared.

References

Acharya UR, Fernandes SL, WeiKoh JE, Ciaccio EJ, Fabell MKM, Tanik UJ, Rajinikanth V, Yeong CH. Automated detection of Alzheimer's disease using brain MRI images- a study with various feature extraction techniques. *J Med Syst*. 2019:43:302.

Arbabshirani MR, Plis S, Sui J, Calhoun VD. Single subject prediction of brain disorders in neuroimaging: promises and pitfalls. *NeuroImage*. 2017:145:137–165.

Bacchi S, Franke K, Wewegama D, Needham E, Patel S, Menon D. Magnetic resonance imaging and positron emission tomography in anti-NMDA receptor encephalitis: a systematic review. *J Clin Neurosci*. 2018:52:54–59.

Bani-Sadr A, Ruitton-Allinieu MC, Brisset JC, Ducray F, Joubert B, Picard G, Cotton F. Contribution of diffusion-weighted imaging to distinguish herpetic encephalitis from auto-immune encephalitis at an early stage. *J Neuroradiol*. 2023:50:288–292.

Barry H, Byrne S, Barrett E, Murphy KC, Cotter DR. Anti-N-methyl-d-aspartate receptor encephalitis: review of clinical presentation, diagnosis and treatment. *BJPsych Bull*. 2015:39:19–23.

Baumgartner A, Rauer S, Hottenrott T, Leypoldt F, Ufer F, Hegen H, Prüss H, Lewerenz J, Deisenhammer F, Stich O. Admission diagnoses of patients later diagnosed with autoimmune encephalitis. *J Neurol*. 2019:266:124–132.

Bernardoni F, King JA, Geisler D, Birkenstock J, Tam FI, Weidner K, Roessner V, White T, Ehrlich S. Nutritional status affects cortical folding: lessons learned from anorexia nervosa. *Biol Psychiatry*. 2018:84:692–701.

Cai L, Liang Y, Huang H, Zhou X, Zheng J. Cerebral functional activity and connectivity changes in anti-N-methyl-D-aspartate receptor encephalitis: a resting-state fMRI study. *Neuroimage Clin*. 2020:25:102189.

Catani M, Dell'Acqua F, Thiebaut de Schotten M. A revised limbic system model for memory, emotion and behaviour. *Neurosci Biobehav Rev*. 2013:37:1724–1737.

Cortes C, Vapnik V. Support-vector networks. *Mach Learn*. 1995:20:273–297.

Dalmau J, Tüzün E, Wu HY, Masjuan J, Rossi JE, Voloschin A, Baehring JM, Shimazaki H, Koide R, King D, et al. Paraneoplastic anti-N-methyl-D-aspartate receptor encephalitis associated with ovarian teratoma. *Ann Neurol*. 2007:61:25–36.

Dalmau J, Gleichman AJ, Hughes EG, Rossi JE, Peng X, Lai M, Dessain SK, Rosenfeld MR, Balice-Gordon R, Lynch DR. Anti-NMDA-receptor encephalitis: case series and analysis of the effects of antibodies. *Lancet Neurol*. 2008:7:1091–1098.

Dalmau J, Lancaster E, Martinez-Hernandez E, Rosenfeld MR, Balice-Gordon R. Clinical experience and laboratory investigations in patients with anti-NMDAR encephalitis. *Lancet Neurol*. 2011:10:63–74.

Dalmau J, Armangué T, Planagumà J, Radosevic M, Mannara F, Leypoldt F, Geis C, Lancaster E, Titulaer MJ, Rosenfeld MR, et al. An update on anti-NMDA receptor encephalitis for neurologists and psychiatrists: mechanisms and models. *Lancet Neurol*. 2019:18: 1045–1057.

Day GS, High SM, Cot B, Tang-Wai DF. Anti-NMDA-receptor encephalitis: case report and literature review of an under-recognized condition. *J Gen Intern Med*. 2011:26:811–816.

de Montmollin E, Demeret S, Brulé N, Conrad M, Dailler F, Lerolle N, Navellou JC, Schwebel C, Alves M, Cour M, et al. Anti-N-methyl-d-aspartate receptor encephalitis in adult patients requiring intensive care. *Am J Respir Crit Care Med*. 2017:195:491–499.

de Pierrefeu A, Löfstedt T, Laidi C, Hadj-Selem F, Bourgin J, Hajek T, Spaniel F, Kolenic M, Ciuciu P, Hamdani N, et al. Identifying a neuroanatomical signature of schizophrenia, reproducible across sites and stages, using machine learning with structured sparsity. *Acta Psychiatr Scand*. 2018:138:571–580.

Demirci O, Clark VP, Calhoun VD. A projection pursuit algorithm to classify individuals using fMRI data: application to schizophrenia. *NeuroImage*. 2008:39:1774–1782.

Finke C, Kopp UA, Prüss H, Dalmau J, Wandinger KP, Ploner CJ. Cognitive deficits following anti-NMDA receptor encephalitis. *J Neurol Neurosurg Psychiatry*. 2012:83:195–198.

Finke C, Kopp UA, Scheel M, Pech LM, Soemmer C, Schlichting J, Leypoldt F, Brandt AU, Wuerfel J, Probst C, et al. Functional and structural brain changes in anti-N-methyl-D-aspartate receptor encephalitis. *Ann Neurol*. 2013:74:284–296.

Finke C, Kopp UA, Pajkert A, Behrens JR, Leypoldt F, Wuerfel JT, Ploner CJ, Prüss H, Paul F. Structural hippocampal damage following anti-N-methyl-D-aspartate receptor encephalitis. *Biol Psychiatry*. 2016:79:727–734.

Gable MS, Gavali S, Radner A, Tilley DH, Lee B, Dyner L, Collins A, Dengel A, Dalmau J, Glaser CA. Anti-NMDA receptor encephalitis: report of ten cases and comparison with VE. *Eur J Clin Microbiol Infect Dis*. 2009:28:1421–1429.

Graus F, Titulaer MJ, Balu R, Benseler S, Bien CG, Cellucci T, Cortese I, Dale RC, Gelfand JM, Geschwind M, et al. A clinical approach to diagnosis of autoimmune encephalitis. *Lancet Neurol*. 2016:15: 391–404.

Hegen H, Uprimny C, Grams A, Virgolini I, Ramberger M, Beer R, Helbok R, Pfausler B, Schmutzhard E. Bi-insular cortical involvement in anti-NMDA-receptor encephalitis - a case report. *BMC Neurol*. 2016:16:130.

Iizuka T, Sakai F, Ide T, Monzen T, Yoshii S, Iigaya M, Suzuki K, Lynch DR, Suzuki N, Hata T, et al. Anti-NMDA receptor encephalitis in Japan: long-term outcome without tumor removal. *Neurology*. 2008:70:504–511.

Iizuka T, Yoshii S, Kan S, Hamada J, Dalmau J, Sakai F, Mochizuki H. Reversible brain atrophy in anti-NMDA receptor encephalitis: a long-term observational study. *J Neurol*. 2010:257:1686–1691.

Iizuka T, Kaneko J, Tominaga N, Someko H, Nakamura M, Ishima D, Kitamura E, Masuda R, Oguni E, Yanagisawa T, et al. Association of progressive cerebellar atrophy with long-term outcome in patients with anti-N-methyl-d-aspartate receptor encephalitis. *JAMA Neurol*. 2016:73:706–713.

Jones BE, Tovar KR, Goehring A, Jalali-Yazdi F, Okada NJ, Gouaux E, Westbrook GL. Autoimmune receptor encephalitis in mice induced by active immunization with conformationally stabilized holoreceptors. *Sci Transl Med*. 2019:11(500):eaaw0044. https://doi.org/10.1126/scitranslmed.aaw0044B1.

Kataoka H, Sawa N, Tonomura Y, Ueno S. Early progression of brain atrophy in patients with anti-N-methyl-D-aspartate receptor encephalitis: case reports. *Medicine (Baltimore)*. 2017:96: e6776.

Kreye J, Wenke NK, Chayka M, Leubner J, Murugan R, Maier N, Jurek B, Ly LT, Brandl D, Rost BR, et al. Human cerebrospinal fluid monoclonal N-methyl-D-aspartate receptor autoantibodies are sufficient for encephalitis pathogenesis. *Brain*. 2016:139: 2641–2652.

Laurikainen H, Isotupa I, Nyman M, Ilonen T, Nummelin T, Salokangas RKR, Hietala J. Longitudinal brain morphology in anti-NMDA receptor encephalitis: a case report with controls. *BMC Psychiatry*. 2019:19:145.

Malviya M, Barman S, Golombeck KS, Planagumà J, Mannara F, Strutz-Seebohm N, Wrzos C, Demir F, Baksmeier C, Steckel J, et al. NMDAR encephalitis: passive transfer from man to mouse by a recombinant antibody. *Ann Clin Transl Neurol*. 2017:4:768–783.

Mo JJ, Zhang JG, Li WL, Chen C, Zhou NJ, Hu WH, Zhang C, Wang Y, Wang X, Liu C, et al. Clinical value of machine learning in the automated detection of focal cortical dysplasia using quantitative multimodal surface-based features. *Front Neurosci*. 2018:12:1008.

Mo J, Liu Z, Sun K, Ma Y, Hu W, Zhang C, Wang Y, Wang X, Liu C, Zhao B, et al. Automated detection of hippocampal sclerosis using clinically empirical and radiomics features. *Epilepsia*. 2019:60: 2519–2529.

Nagels A, Cabanis M, Oppel A, Kirner-Veselinovic A, Schales C, Kircher T. S-ketamine-induced NMDA receptor blockade during natural speech production and its implications for formal thought disorder in schizophrenia: a Pharmaco-fMRI study. *Neuropsychopharmacology*. 2018:43:1324–1333.

Newcomer JW, Farber NB, Olney JW. NMDA receptor function, memory, and brain aging. *Dialogues Clin Neurosci*. 2000:2:219–232.

Orrù G, Pettersson-Yeo W, Marquand AF, Sartori G, Mechelli A. Using support vector machine to identify imaging biomarkers of neurological and psychiatric disease: a critical review. *Neurosci Biobehav Rev*. 2012:36:1140–1152.

Paoletti P, Bellone C, Zhou Q. NMDANMDA receptor subunit diversity: impact on receptor properties, synaptic plasticity and disease. *Nat Rev Neurosci*. 2013:14:383–400.

Peer M, Prüss H, Ben-Dayan I, Paul F, Arzy S, Finke C. Functional connectivity of large-scale brain networks in patients with anti-NMDA receptor encephalitis: an observational study. *Lancet Psychiatry*. 2017:4:768–774.

Pessoa L, Hof PR. From Paul Broca's great limbic lobe to the limbic system. *J Comp Neurol*. 2015:523:2495–2500.

Phillips OR, Joshi SH, Narr KL, Shattuck DW, Singh M, Di Paola M, Ploner CJ, Prüss H, Paul F, Finke C. Superficial white matter damage in anti-NMDA receptor encephalitis. *J Neurol Neurosurg Psychiatry*. 2018:89:518–525.

Shives KD, Tyler KL, Beckham JD. Molecular mechanisms of neuroinflammation and injury during acute VE. *J Neuroimmunol*. 2017:308: 102–111.

Singh TD, Fugate JE, Rabinstein AA. The spectrum of acute encephalitis: causes, management, and predictors of outcome. *Neurology*. 2015:84:359–366.

Sonneville R, Gault N, de Montmollin E, Klein IF, Mariotte E, Chemam S, Tubach F, Mourvillier B, Timsit JF, Wolff M, et al. Clinical spectrum and outcomes of patients with encephalitis requiring intensive care. *Eur J Neurol*. 2015:22:6, e11–16.

Taguchi Y, Takashima S, Nukui T, Tanaka K. Reversible "brain atrophy" in anti-NMDA receptor encephalitis. *Intern Med*. 2011: 50:2697.

Tan Y, Liu M, He L. Clinical and MRI differential analysis of autoimmune encephalitis and VE. *J Taibah Univ Med Sci*. 2023:18: 271–278.

Thakur KT, Motta M, Asemota AO, Kirsch HL, Benavides DR, Schneider EB, McArthur JC, Geocadin RG, Venkatesan A. Predictors of outcome in acute encephalitis. *Neurology*. 2013:81: 793–800.

Titulaer MJ, McCracken L, Gabilondo I, Armangué T, Glaser C, Iizuka T, Honig LS, Benseler SM, Kawachi I, Martinez-Hernandez E, et al. Treatment and prognostic factors for long-term outcome in patients with anti-NMDA receptor encephalitis: an observational cohort study. *Lancet Neurol*. 2013:12:157–165.

Torrico TJ, Abdijadid S, Salah Aboubakr (eds). Neuroanatomy, limbic system. In: *StatPearls Treasure Island*. FL: StatPearls Publishing; 2020. Copyright © 2020, StatPearls Publishing LLC.

Tüzün E, Zhou L, Baehring JM, Bannykh S, Rosenfeld MR, Dalmau J. Evidence for antibody-mediated pathogenesis in anti-NMDAR encephalitis associated with ovarian teratoma. *Acta Neuropathol*. 2009:118:737–743.

Venkatesan A, Adatia K. Anti-NMDA-receptor encephalitis: from bench to clinic. *ACS Chem Neurosci*. 2017:8:2586–2595.

Venkatesan A, Tunkel AR, Bloch KC, Lauring AS, Sejvar J, Bitnun A, Stahl JP, Mailles A, Drebot M, Rupprecht CE, et al. Case definitions, diagnostic algorithms, and priorities in encephalitis: consensus statement of the international encephalitis consortium. *Clin Infect Dis*. 2013:57:1114–1128.

Wang C, Zheng D, Xu J, Lam W, Yew DT. Brain damages in ketamine addicts as revealed by magnetic resonance imaging. *Front Neuroanat*. 2013:7:23.

Xiang Y, Zeng C, Liu B, Tan W, Wu J, Hu X, Han Y, Luo Q, Gong J, Liu J, et al. Deep learning-enabled identification of autoimmune encephalitis on 3D multi-sequence MRI. *J Magn Reson Imaging*. 2022:55:1082–1092.

Xu J, Guo Y, Li J, Lv X, Zhang J, Zhang J, Hu Q, Wang K, Tian Y. Progressive cortical and sub-cortical alterations in patients with anti-N-methyl-D-aspartate receptor encephalitis. *J Neurol*. 2022:269:389–398.

Yassin W, Nakatani H, Zhu Y, Kojima M, Owada K, Kuwabara H, Gonoi W, Aoki Y, Takao H, Natsubori T, et al. Machine-learning classification using neuroimaging data in schizophrenia, autism, ultra-high risk and first-episode psychosis. *Transl Psychiatry*. 2020:10:278.